

Figs. E1 to E10

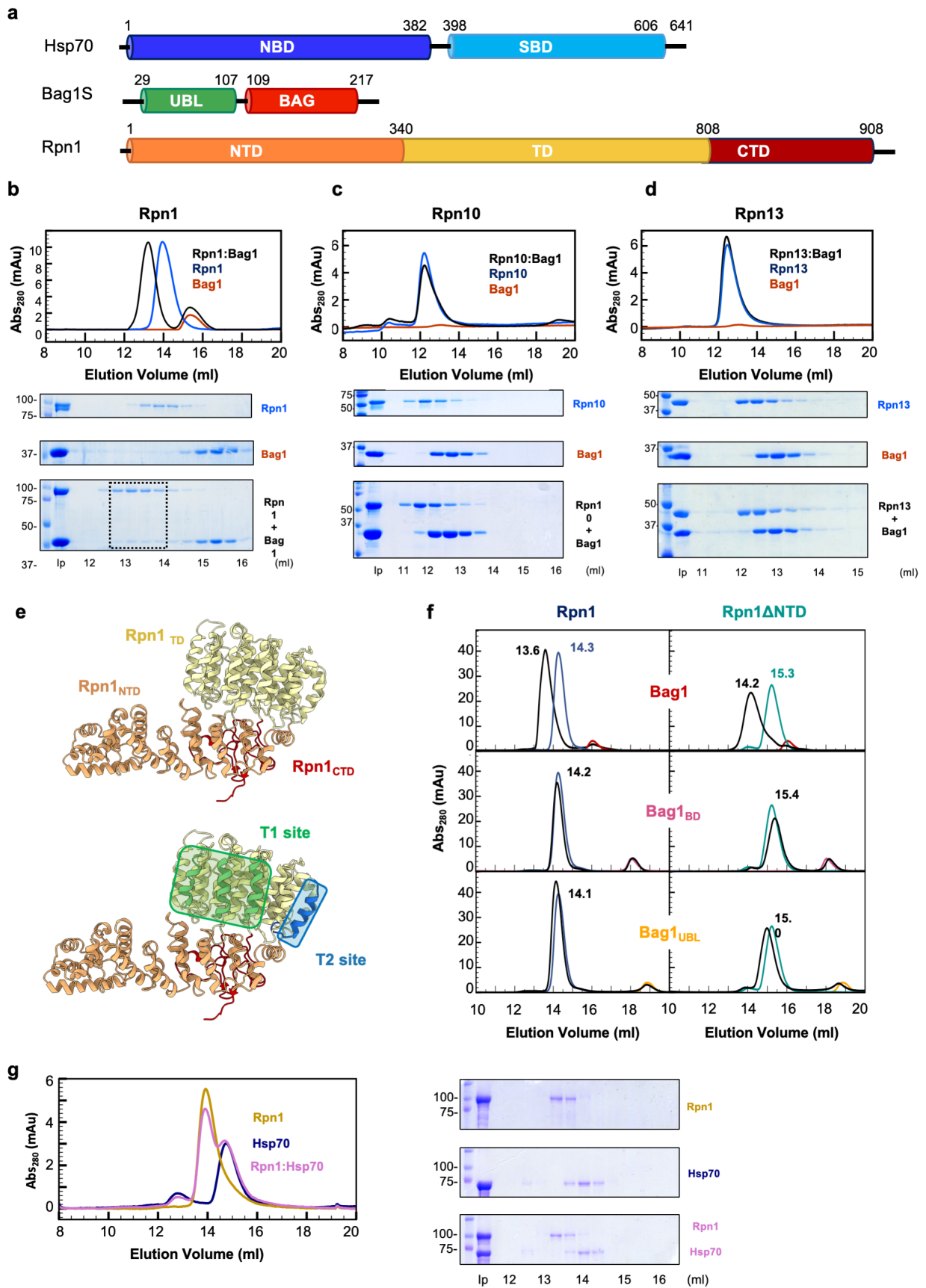


Fig. E1. Domain structure and SEC analysis of the Bag1-Rpn1 interaction. (a) Domain structures of the chaperone Hsp70, the cochaperone Bag1, and the proteasomal subunit Rpn1. (b-d) SEC and SDS-PAGE analysis to identify the proteasome binding subunit of Bag1. Bag1 was incubated with the proteasome ubiquitin receptors Rpn1 (b), Rpn10 (c) and Rpn13 (d) and then subjected to the SEC column. Only Rpn1 (b) shows a peak shift in the presence of Bag1, indicating the formation of a dimeric complex. (e) Structure of Rpn1 highlighting its domain structures (upper panel). Rpn1_{TD}, Rpn1_{NTD} and Rpn1_{CTD} are colored in light yellow, orange and red, respectively (PDB: 7W3K). T1 ubiquitin binding site (Chen et al., 2016), and T2 UBL binding site (Shi et al., 2016) are highlighted in green and blue, respectively (lower panel). (f) Rpn1 interacts with the UBL domain of Bag1 (Bag1_{UBL}) but not the BAG domain (Bag1_{BD}). Deletion of the N-terminal region of Rpn1 (Rpn1_{NTD}) did not interfere with Bag1 binding, suggesting that Bag1_{UBL} interacts with Rpn1_{TD} but not Rpn1_{NTD}. SEC analysis to identify the domain specificity revealed a stable interaction between full-length Bag1 and Rpn1. (g) SEC analysis showed no peak shift when mixing Rpn1 and Hsp70, indicating no direct interaction between Rpn1 and Hsp70.

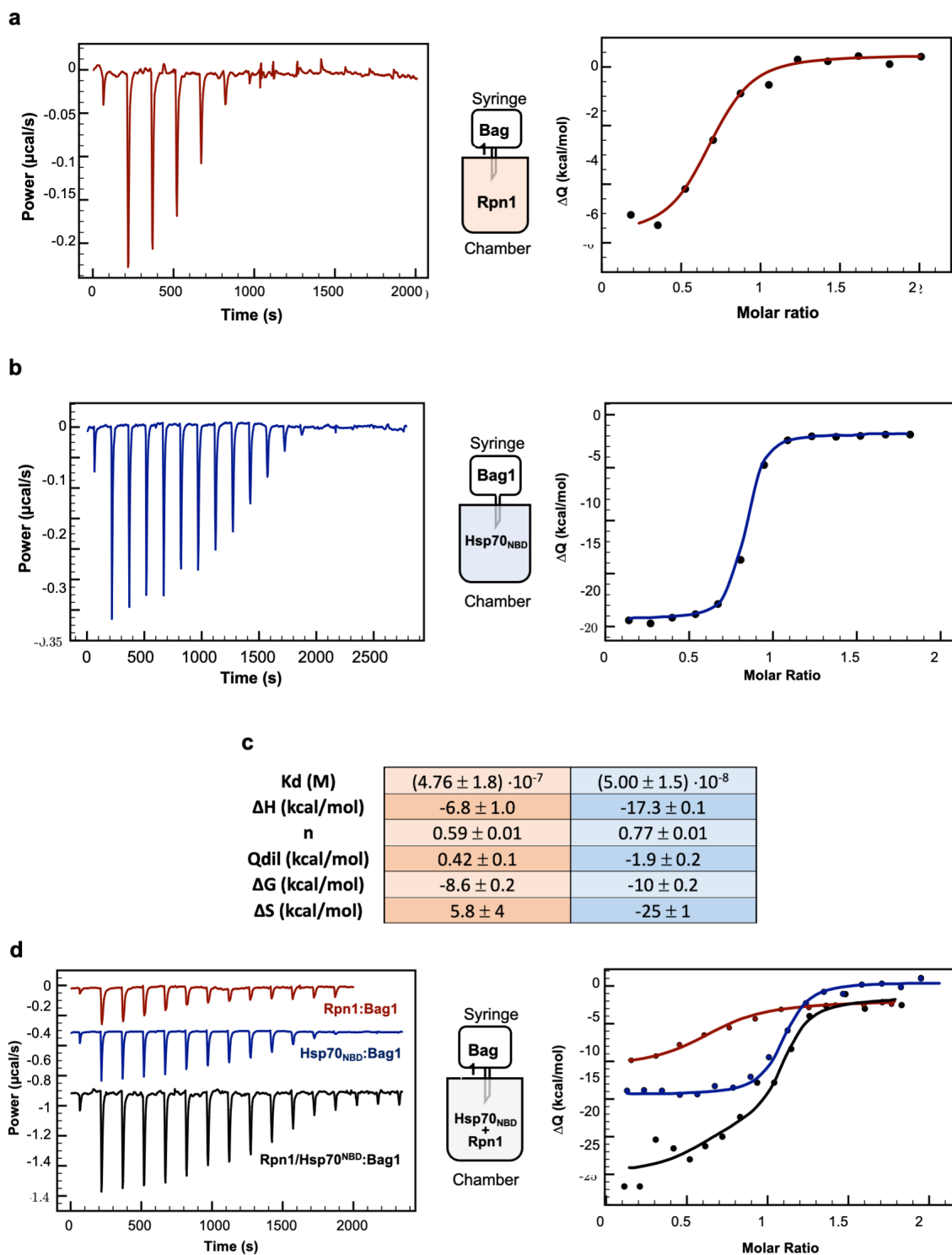


Fig. E2. Isothermal titration calorimetry (ITC) experiment for Rpn1, Hsp70 and a mixture of Rpn1-Hsp70 titrated with Bag1. Panels of the raw data (left) and fitted integrated data (right) of the titration experiments where Bag1 was titrated with Rpn1 (a), Hsp70_{NBD} (b). An experimental schematic is shown between panels. All ITC binding assays were performed with an PEAQ-ITC microcalorimeter (Malvern) at 25 °C in a buffer containing 20 mM phosphate buffer pH 7.4 and 150 mM KCl, and data were analyzed using the AFFINImeter software. (c) Summary of the thermodynamic parameters of Rpn1:Bag1 (salmon column on the left) and Hsp70_{NBD}:Bag1 (blue column on the right), derived from the one-to-one binding model. Averages over multiple measurements are listed. (d) ITC assay for the ternary complex with Bag1 titrated against a mixture of Rpn1 and Hsp70_{NBD}. The curve was fitted simultaneously with binary complexes assuming independent binding of Hsp70_{NBD} and Rpn1 to Bag1. The black trace in (d) represents the simulated formation of the ternary complex of Hsp70_{NBD}:Bag1:Rpn1, compared to the binding parameters in (c). The individual plots for Bag1 titrated with Rpn1 and Hsp70 are also shown in red and blue, respectively.

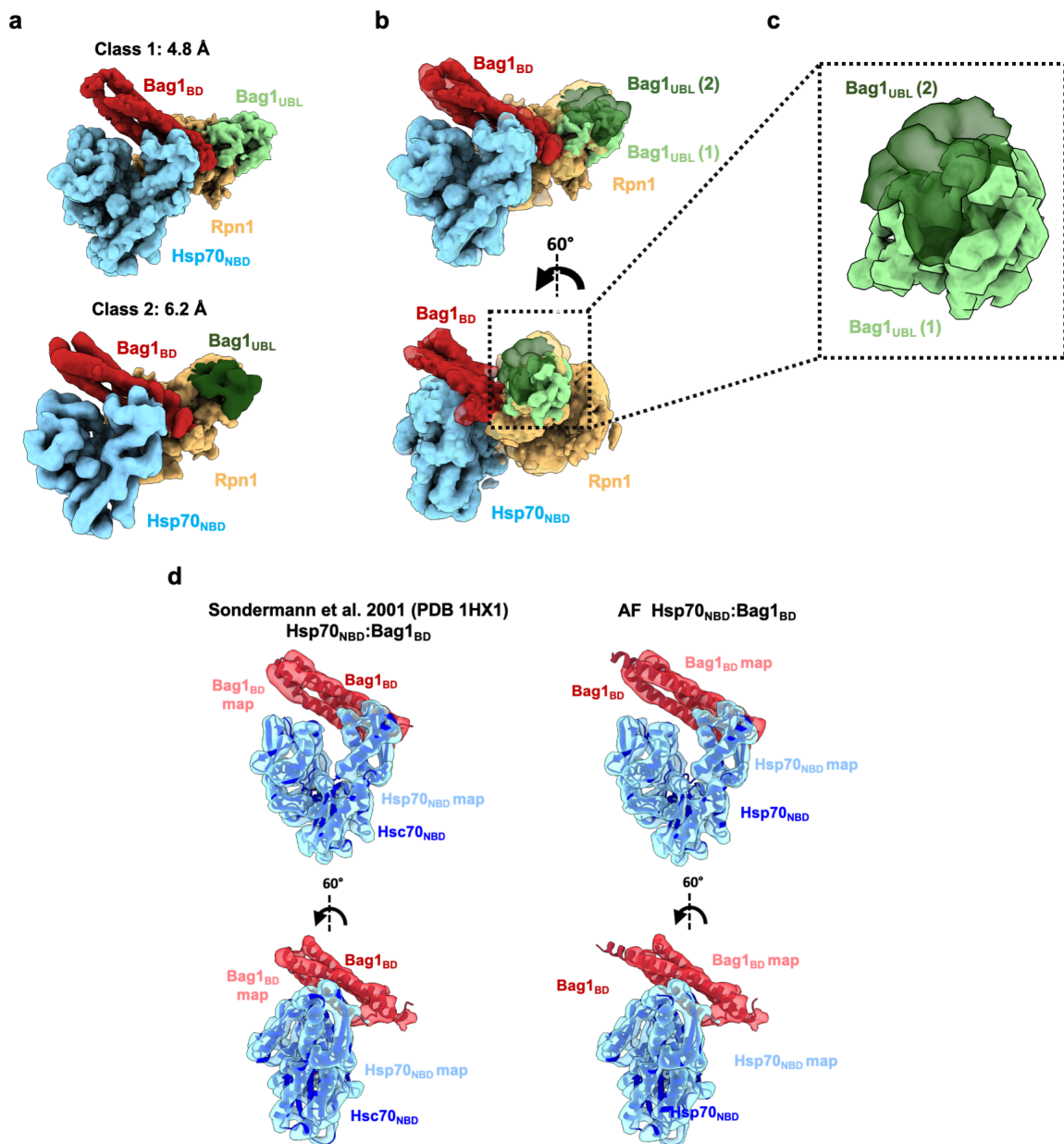


Fig. E3. 3D reconstructions of the Hsp70_{NBD}:Bag1:Rpn1 ternary complex. (a) Cryo-EM density maps of the Hsp70_{NBD}:Bag1:Rpn1 ternary complex (Class 1 EMDB: 52195; Class 2 EMDB: 52196). Rpn1, Bag1_{BD} and Hsp70_{NBD} are colored in beige, red and blue, respectively in both maps. The Bag1_{UBL} from Class 1 is depicted in light green and in dark green for Class 2. (b) An overlay of the two maps reveals their structural similarity, with the exception of the Bag1_{UBL} domain, which displays structural flexibility (c). (d) Comparison of the Hsp70_{NBD}:Bag1_{BD} interaction (blue:red) in the context of the ternary complex. Crystal structure of Hsc70_{NBD}:Bag1_{BD} (PDB: 1HX1, Sondermann *et al.*, 2001) (left) and an AlphaFold prediction, showing no noticeable differences (right). All structures were docked into the cryo-EM map of the Hsp70_{NBD}:Bag1:Rpn1 ternary complex.

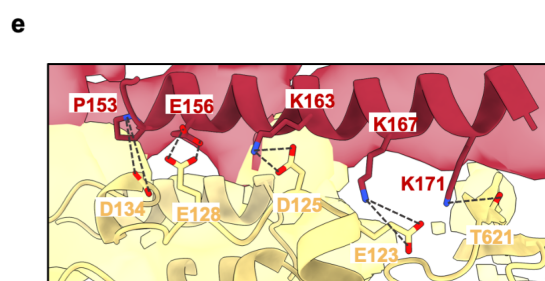
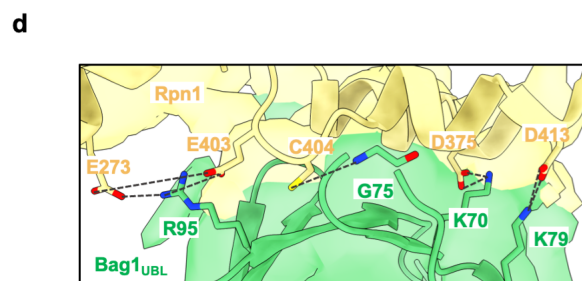
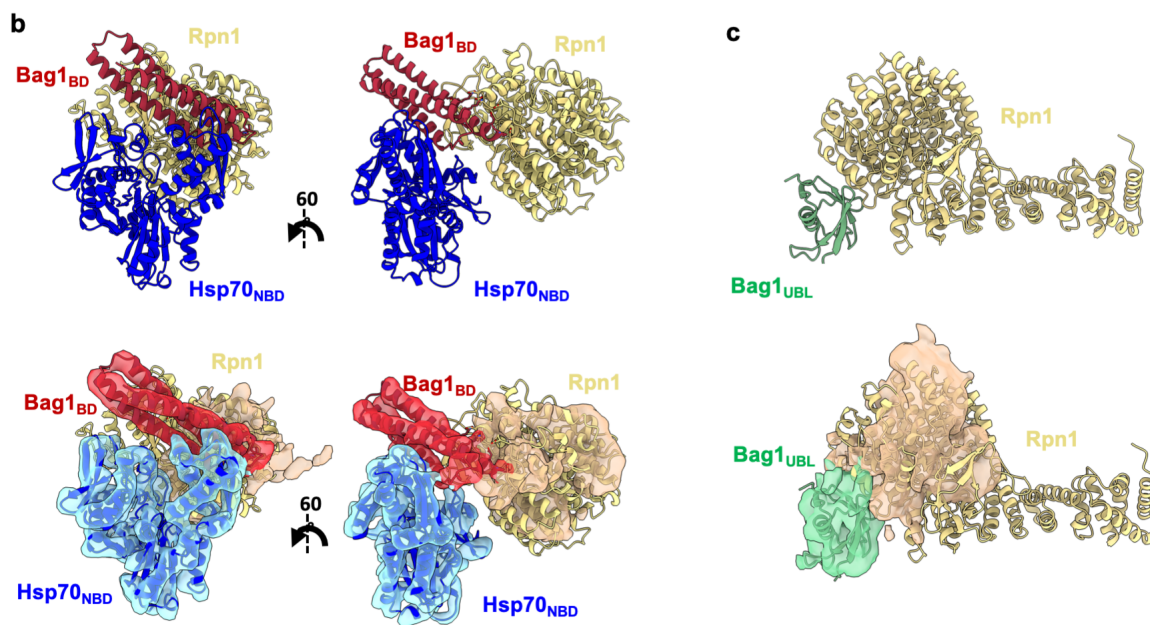
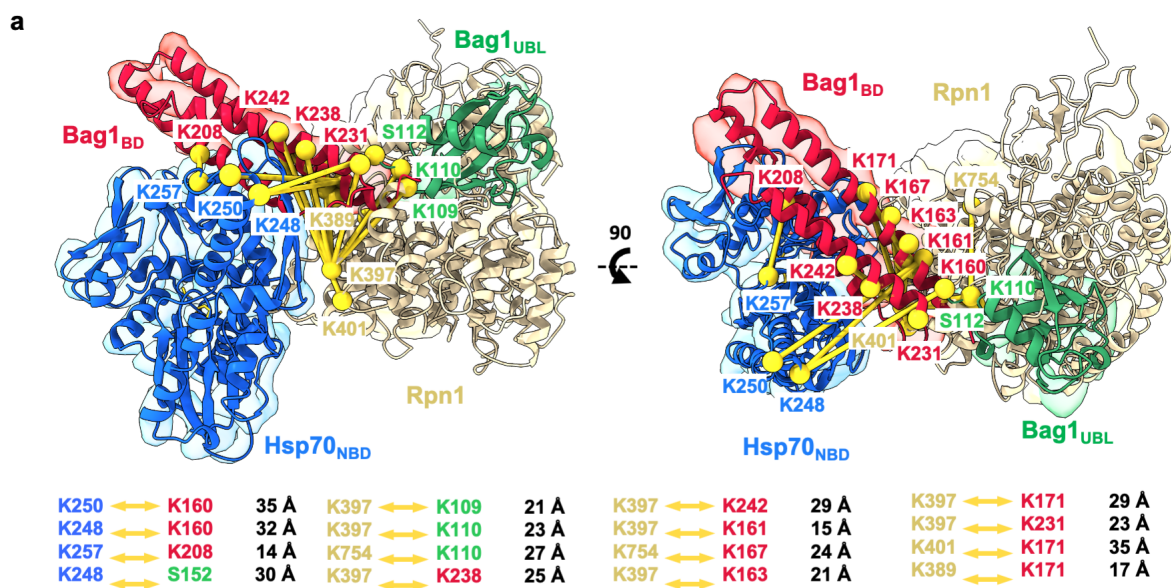


Fig. E4. Structural validation of the Hsp70_{NBD}:Bag1:Rpn1 ternary complex. (a) Two views of the ternary complex reconstruction incorporating cross-links (yellow) identified through XL-MS analysis. The distances of all cross-links calculated from the structural model (rigid body fitting of atomic model of PDB: 1HX1) are also indicated. (b) AlphaFold prediction of Rpn1:Bag1_{BD}:Hsp70_{NBD} complex (upper panel) fitted into our cryo-EM reconstruction of the ternary complex (EMDB: 52195) (lower panel). (c) AlphaFold prediction of the Rpn1:Bag1_{UBL} complex (upper panel) fitted into our cryo-EM reconstruction of the ternary complex (EMDB: 52195) (lower panel). AlphaFold predicted contacts between Rpn1:Bag1_{UBL} (c) and Rpn1:Bag1_{BD} (d). Putative binding interfaces extracted from the predictions stated above. Color code follows Rpn1 in beige/yellow, Bag1_{UBL} in green, Bag1_{BD} in red and Hsp70_{NBD} in blue.

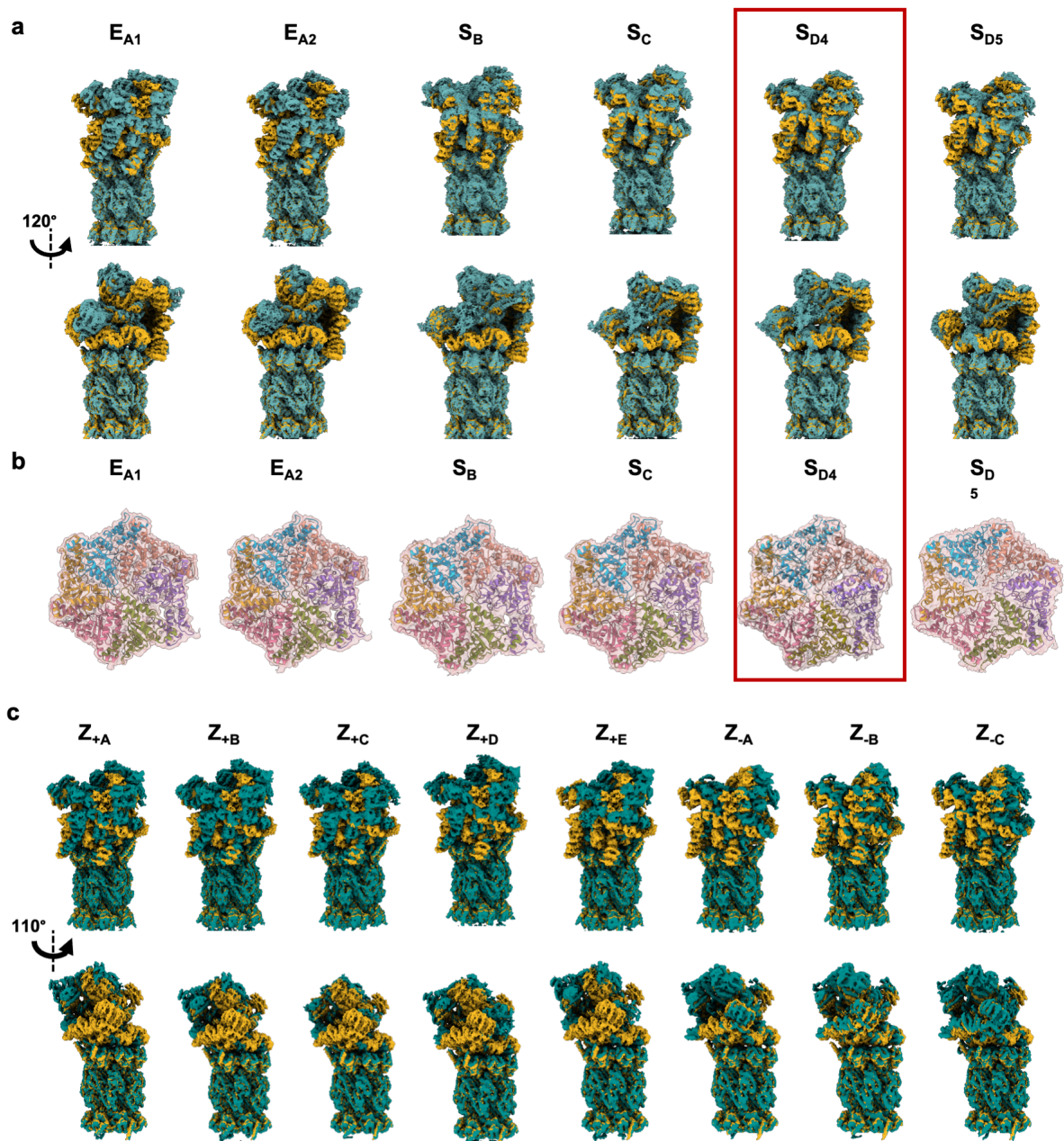


Fig. E5. Structural comparison of the Bag1-bound 26S proteasome with reported human 26S proteasome structures. (a) Structural comparison of the cryo-EM reconstruction of 26S proteasome in S_{BAG1} state (goldenrod) with previously reported cryo-EM reconstructions of USP14-bound 26S proteasome (teal). Cryo-EM maps from Zhang et al. (Zhang, Zou et al. 2022) were used for comparison: E_{A1} (EMDB: 32272), E_{A2} (emdb: 32273), S_B (EMDB: 32281), S_C (EMDB: 32282), S_{D4} (EMDB: 32283), S_{D5} (EMDB: 32284). (b) Cryo-EM segmentation of the ATPase ring in previously reported structures of the USP14-bound 26S proteasome. Different from the Bag1-bound 26S proteasome structures, the tight packing of the ATPase rings was observed in all canonical structures. (c) Structural comparison of the cryo-EM reconstruction of 26S proteasome in S_{BAG1} state (goldenrod) with previously reported cryo-EM reconstructions of the ZFAND5-bound 26S proteasome (teal). Cryo-EM maps from Lee et al. (Lee et al. 2023) were used for comparison: Z_{+A} (EMDB: 14201), Z_{+B} (EMDB: 14202), Z_{+C} (EMDB: 14203), Z_{+D} (EMDB: 14204), Z_{+E} (EMDB: 14205), Z_{-A} (EMDB: 14209), Z_{-B} (EMDB: 14210), Z_{-C} (EMDB: 14212).

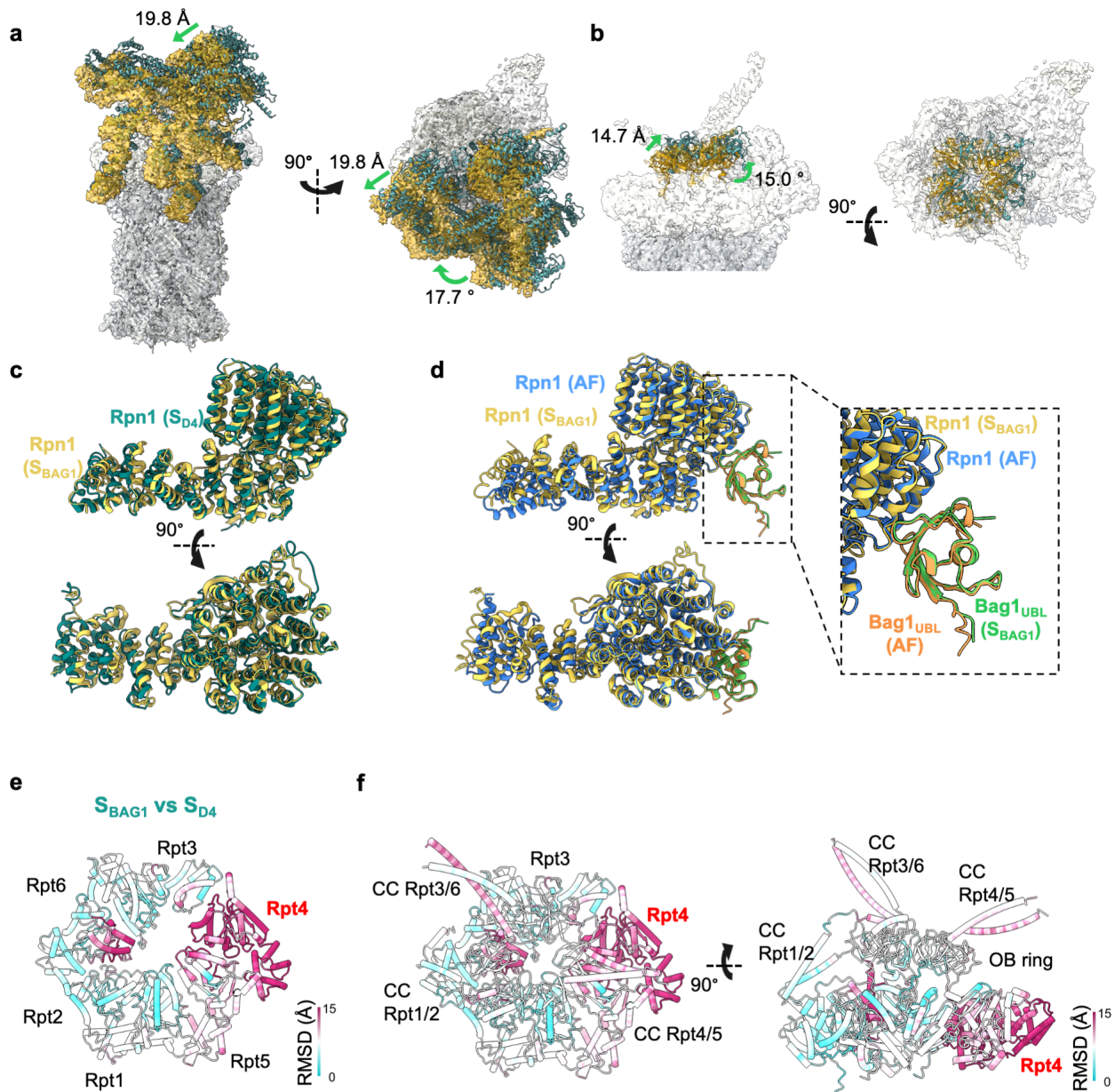


Fig. E6. Structural comparison of the cryo-EM reconstruction of the 26S proteasome in S_{BAG1} state with S_{D4} state. Structural comparison of the cryo-EM reconstruction of the 26S proteasome in S_{BAG1} (EMDB: 52097 in goldenrod) with the S_{D4} state (PDB: 7W3K in teal), focusing on the lid subcomplex (a) and OB ring (b). The rest of densities are shown in light grey. The Changes in shift (Å) and angle ($^{\circ}$) are indicated. (c) Structural comparison of Rpn1 in S_{BAG1} (goldenrod) and S_{D4} (blue green) states. No significant conformational change was observed in Rpn1. (d) Structural comparison of the Rpn1 at the Bag1_{UBL} interface in S_{BAG1} (goldenrod) with AlphaFold prediction (blue). Bag1_{UBL} is shown in green (S_{BAG1}) and orange (S_{D4}), respectively. (e,f) Residue-wise RMSD of the Rpt subunits calculated from the main chain including N, C α , C, O between S_{BAG1} and S_{D4} states. Residue-wise RMSDs of the main-chain of the ATPase domain (e) and whole Rpt subunits (f), compared the difference from S_{BAG1} with S_{D4} (PDB: 7W3K), illustrates the extent of the conformational shift caused by Bag1-binding (in Å). Two structures are aligned to the α ring of the CP. The RMSD is plotted on the S_{BAG1} structure. Rpt4 (large, small domains), Rpt5 (large), Rpt3 (small) and Rpt6 (large) shows large shifts in the ATPase ring. The coiled-coil (CC) of the Rpt3/6 and Rpt4/5 are displaced compared to the Rpt1/2 CC.

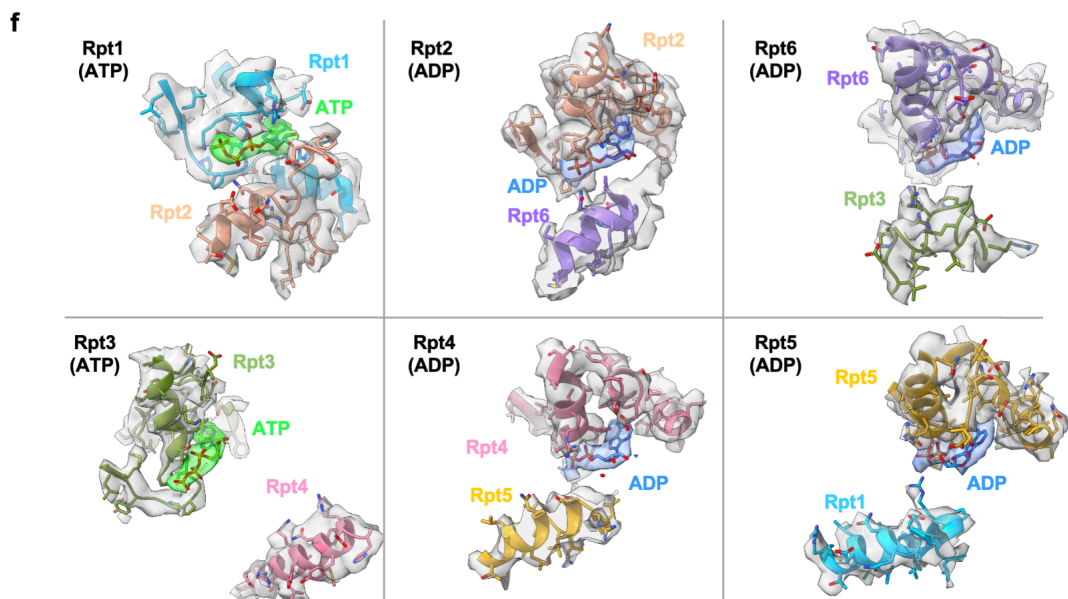
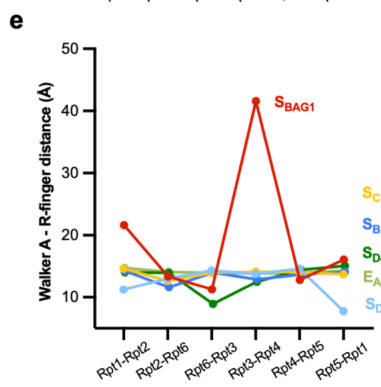
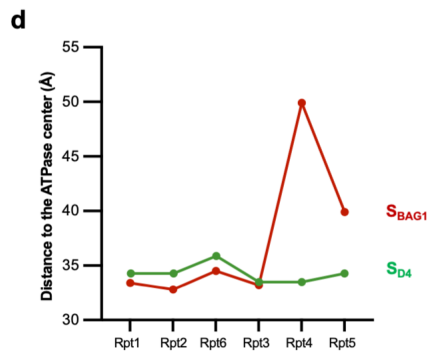
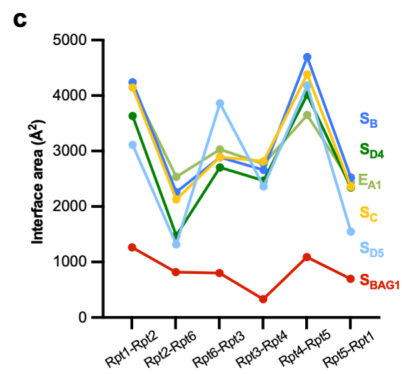
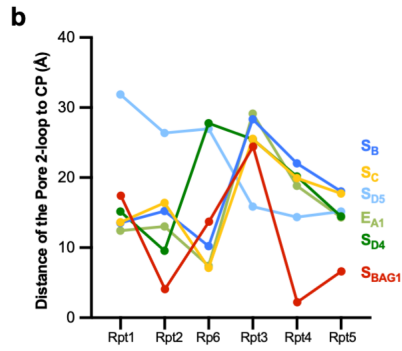
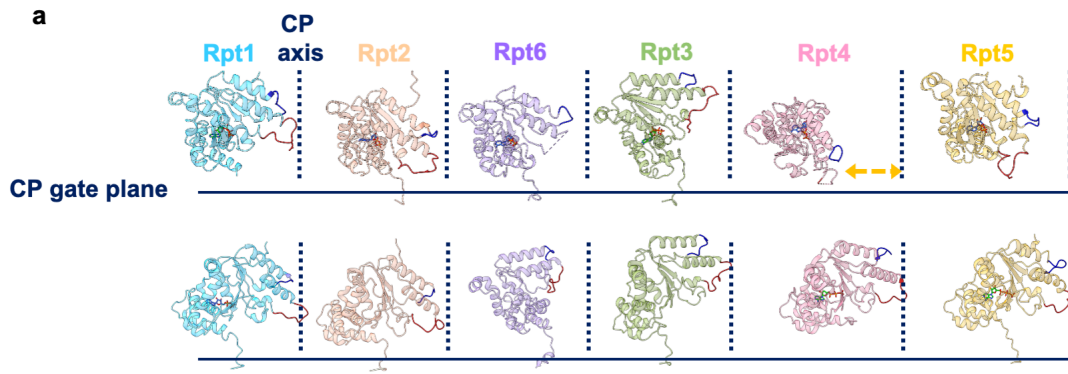


Fig. E7. Structural analysis of the ATPase Rpt subunits in S_{BAG1} . (a) Organization of the AAA+ ATPase and interaction with the CP. Individual Rpt subunits in S_{BAG1} (upper panel, PDB: 9HEU) and S_{D4} (lower panel, PDB: 7W3K) rotated around the CP axis are shown in approximately 60° steps. Due to the deformation of the ring structure, orientation of each subunit in S_{BAG1} is adjusted to properly show the side view and pore-2 loop. The positions of the CP axis and CP plane of the gate are shown as dotted lines and solid lines, respectively. Pore-1 loops and Pore-2 loops of each subunit are highlighted in blue and red, respectively. The Bag1-induced conformational change alters the position of Rpt4 subunit far away from the central axis. (b) Plot of distances between the closest α carbon of the Pore-2 loops to the plane of the CP gate. Pore-2 loops in Rpt2, Rpt4 and Rpt5 in S_{BAG1} are close to the CP plane compared to any of reported structures (E_{A1} , S_B , S_C , S_{D4} , S_{D5}) (Zhang, Zou et al. 2022). (c) Contact area between the large AAA+ domains of neighboring Rpt subunits in S_{BAG1} and the reported states (E_{A1} , S_B , S_C , S_{D4} , S_{D5}) (Zhang, Zou et al. 2022). All interfaces in S_{BAG1} shows small contact interface. (d) Distance of the centroid of individual subunits to the axis of the ATPase ring in S_{BAG1} and S_{D4} . Rpt4 is completely off the axis as it is shown in Figure 3g. (e) Opening of the nucleotide-binding pockets in S_{BAG1} and the reported states (E_{A1} , S_B , S_C , S_{D4} , S_{D5}) (Zhang, Zou et al. 2022). The distances between the α carbon of Walker-A Thr residue and the α carbon of the Arg finger of the neighboring subunit are shown. The interface between Rpt3 and Rpt4 in S_{BAG1} is especially opened. (f) Detailed views of individual Rpt nucleotide-binding pockets, together with the adjacent Rpt subunit. Nucleotide binding pocket of a subunit and the closest α helix of the neighboring subunit are shown. In Rpt1 and Rpt3 pockets, ATP densities are observed, while ADP was observed in Rpt2, 4, 5 and 6.

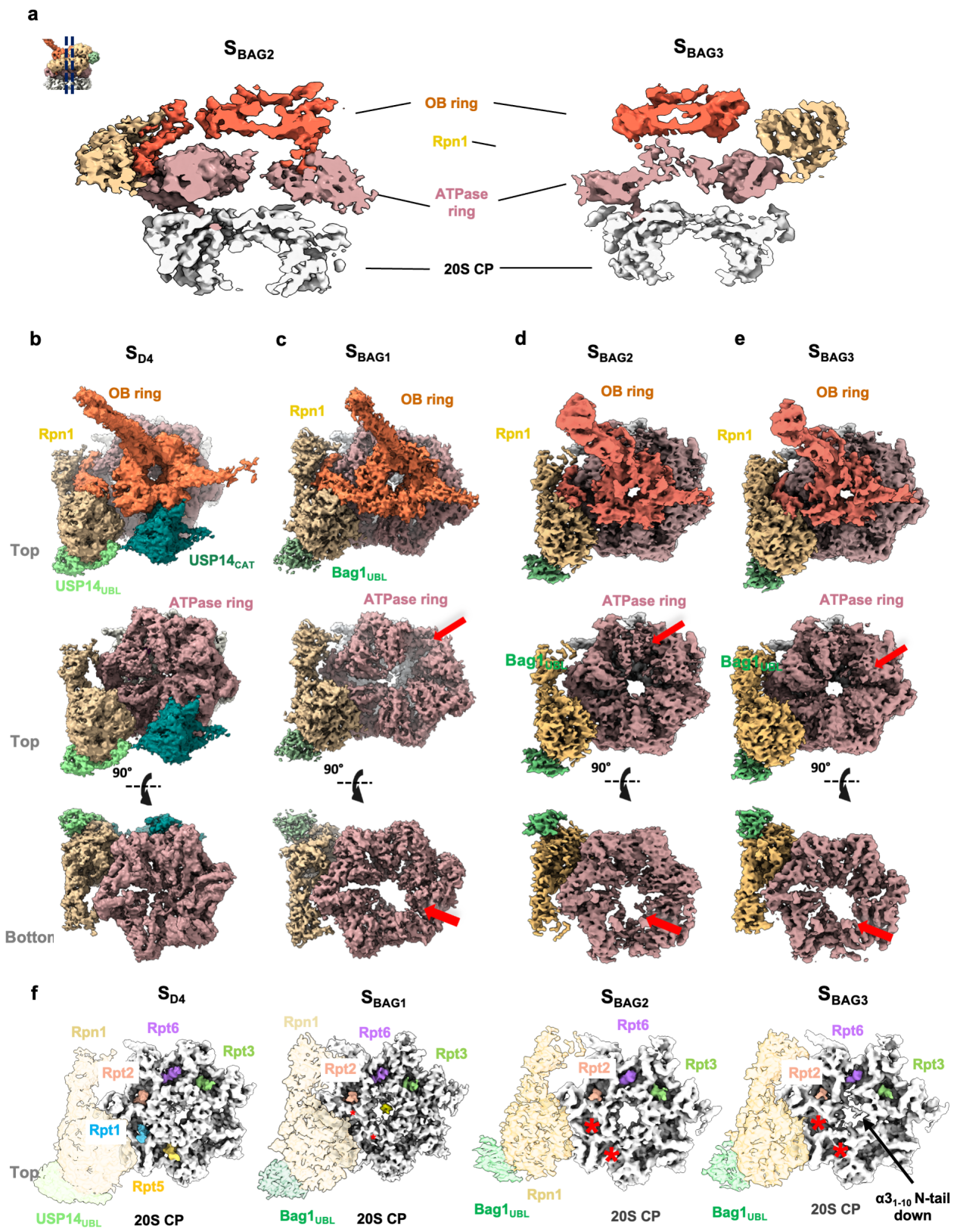


Fig. E8. Cryo-EM segmentations of the 26S proteasome in S_{D4} and S_{BAG1-3} . (a) Cross-sections of cryo-EM maps in S_{BAG2} (left panel) and S_{BAG3} (right panel) in the same orientation and color with Figure 4a, focusing on the interface between the ATPase and CP rings. The color codes are as follows; OB ring (orange), ATPase ring (rosy brown), 20S (white) and Rpn1 (beige). In both S_{BAG2} and S_{BAG3} structures, a significant cavity is created in the ATPase domain as it is observed in S_{BAG1} . (b-e) Structural comparison of the cut-away views of the USP14-bound 26S proteasome (S_{D4}) (EMDB: 32282) (b), Bag1-bound 26S proteasome in S_{BAG1} (EMDB: 52097) (c), Bag1-bound 26S proteasome in S_{BAG2} (EMDB: 52193) (d) and in S_{BAG3} (EMDB: 52194) (e). The same color codes are used as in panel (a). Each segment is shown down the long axis of the 26S proteasome from the OB ring (top) and the ATPase domain ring (top view; middle and bottom view; bottom). Large cavities are observed at the center of the ATPase ring in all three S_{BAG} conformations. (f) Insertion of Rpt C-terminal tails into CP α ring pockets. The top views of the 20S CP, Rpn1, as well as Bag1_{UBL} domains are shown in white, tan, and light green, respectively. The C-terminal Rpt densities inserted into the CP are colored in Rpt1 in deep sky blue, Rpt2 in salmon pink, Rpt6 in purple, Rpt3 in olive green, and Rpt5 in goldenrod. Only three C-terminal Rpt tails (Rpt2, Rpt3, Rpt5) are inserted into CP α pockets in S_{BAG} conformations.

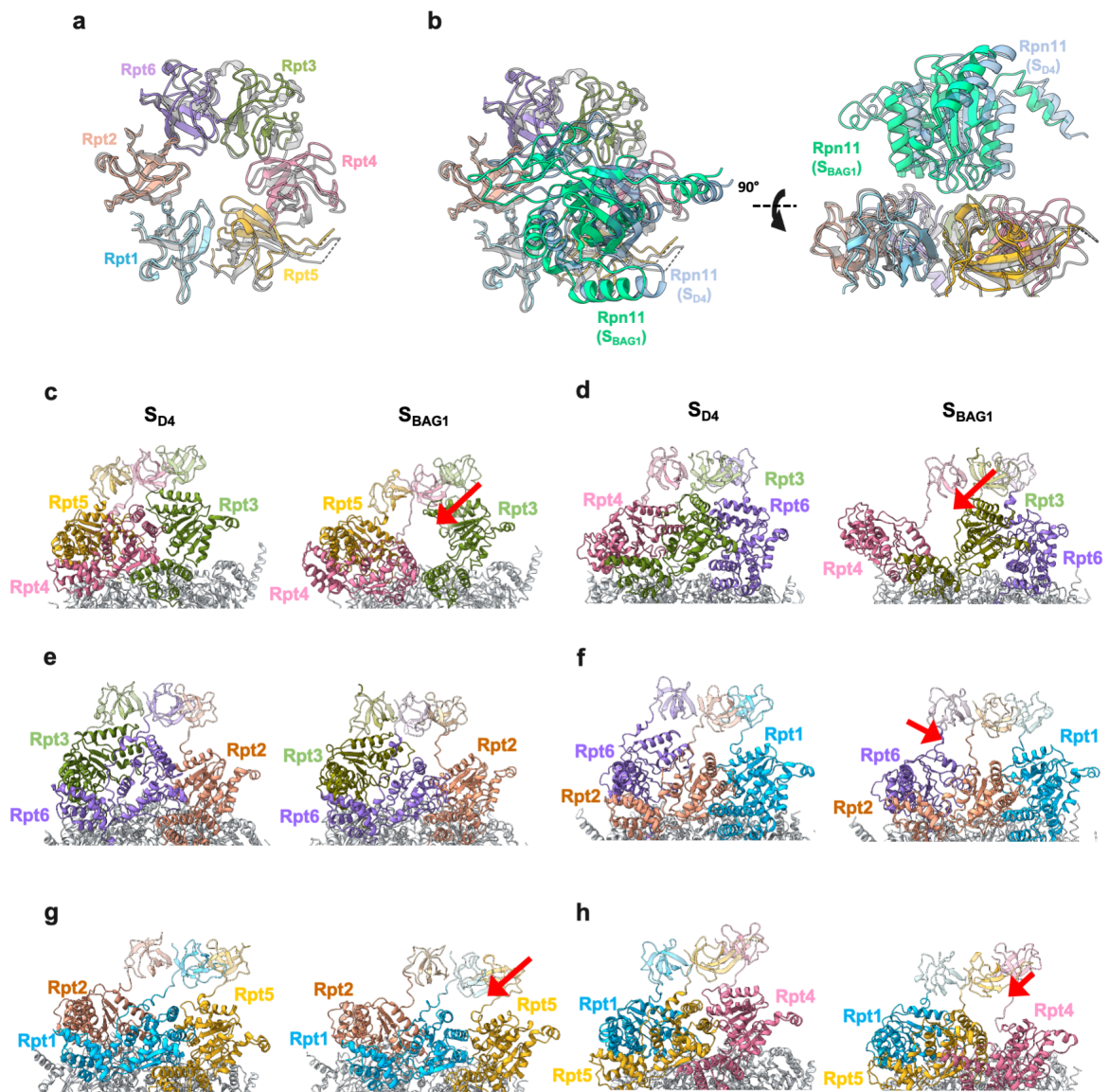


Fig. E10. The Interfaces between OB and ATPase rings in S_{BAG1} and S_{D4} are compared. Structural comparisons between S_{D4} (PDB: 7W3K) and S_{BAG1} (PDB: 9HEU) and, focusing on the OB domains (a) and Rpn11 (b). No significant changes between both states are observed in the OB ring. Rpt subunits of S_{BAG1} are colored with Rpn1 in deep sky blue, Rpt2 in salmon pink, Rpt6 in purple, Rpt3 in olive green, Rpt4 in pink and Rpt5 in goldenrod, whereas S_{D4} subunits are in gray. Rpn11 is depicted in turquoise for S_{BAG1} and light blue for S_{D4} . (c-h) Comparison of the OB-ATPase interfaces formed by three sequential Rpt subunits. The interfaces are shown in every 60° step. Rpt1, Rpt2, Rpt6, Rpt3, Rpt4 and Rpt5 are shown in deep sky blue, salmon, purple, olive green, pink and goldenrod. 20S CP is shown in white. The OB domains are shown in transparent. Opened interfaces of the OB-ATPase ring are highlighted by red arrows. Due to the significant conformational change of the ATPase domains, a large opening is created at the interface between OB and ATPase rings.